Submitted to the Journal of Alloys and Compounds

Determination of hydrogen compatibility for Cu-Al-Ni-Fe-Mn cast alloys prepared by varying Al and Ni contents

Junichiro Yamabe[a,b,e]*, Ren Yoshimoto[a], Kentaro Wada[c], Takafumi Yano[d], Kojiro Fujiyama[d], Takashi Iijima[e], Hirotoshi Enoki[e]

[a] Department of Mechanical Engineering, Fukuoka University, 8-19-1 Nanakuma, Jonan-ku, Fukuoka 814-0180, Japan

[b] Research Institute of Materials Science and Technology, Fukuoka University, 8-19-1 Nanakuma, Jonan-ku, Fukuoka 814-0180, Japan

[c] National Institute for Materials Science, 1-2-1 Sengen, Tsukuba, Ibaraki 305-0047, Japan

[d] Takatori Seisakusho Co., Ltd., 213-1 Yoshiimachi, Ukiha, Fukuoka 839-1321, Japan

[e] Global Zero Emission Research Center, National Institute of Advanced Industrial Science and Technology (AIST), 16-1 Onogawa, Tsukuba, Ibaraki 305-8569, Japan

*Corresponding author

Abstract

Hydrogen compatibility of Cu-Al-Ni-Fe-Mn cast alloys was investigated via slow strain rate tensile tests in high-pressure hydrogen gas. Four types of alloys were prepared by varying the Al and/or Ni contents. Larger Al and Ni contents resulted in more elongated microstructures with smaller grains and more precipitates, respectively. The tensile strength of the alloys increased with larger Al and/or Ni contents, whereas the ductility decreased only by adding a larger amount of Al. The maximum tensile strength was produced by adding larger amounts of both Al and Ni, which was fairly higher than those of stable austenitic stainless steels. Despite the difference in the microstructures and tensile strengths of the alloys, the hydrogen contents and hydrogen diffusivities showed no substantial difference. Additionally, their reduction in area measured after the tensile tests was not degraded by the high-pressure hydrogen gas, revealing an excellent resistance to hydrogen embrittlement.

Keywords: Hydrogen embrittlement; Aluminum bronze; Casting; High-pressure hydrogen; Hydrogen uptake; Diffusivity

1. Introduction

Global warming is a serious issue that must be actively addressed to achieve worldwide carbon neutrality. The recent social demand for environmental conservation has accelerated research on hydrogen embrittlement (HE), a phenomenon whereby dissolved hydrogen in metals degrades their tensile strength (TS) and ductility. The degree of HE in various metallic materials is generally evaluated via slow strain rate tensile (SSRT) testing [1–13].

The materials used for high-pressure hydrogen components such as hydrogen stations (HSs) and fuel cell vehicles (FCVs) are exposed to high-pressure hydrogen gas at around 100 MPa. Since the ductility of many materials is degraded by hydrogen, Japanese regulations stipulate that only materials that are negligibly embrittled by hydrogen are to be used in high-pressure hydrogen components to ensure safety [14]. In this context, only stable austenitic stainless steels, Types 316 and 316L, with high nickel-equivalent values [15,16] are authorized for use in high-pressure hydrogen gas environments. These austenitic stainless steels are often referred to as nickel-equivalent materials. However, such nickel-equivalent materials are low in strength and high in cost. Therefore, to achieve widespread use of HSs and FCVs, it is necessary to develop low-cost, high-strength materials without compromising the resistance to HE. Alternatively, it may be necessary to construct reasonable material selection [17,18] and strength design [19–21] methods in consideration of HE. Regarding the materials used for FCVs adopting an infinite life design (i.e., fatigue limit design), a new material selection method that enables the use of Type 304 stainless steel is being discussed on the basis that the hydrogen does not degrade the fatigue limit of the material, although it does degrade the SSRT properties.

Regarding materials with high resistance to HE, a high-strength stainless steel with a large amount of N added [22] and a low-Mo steel to contribute to resource saving [23] have been developed. On the other hand, Yamabe et al. [24] and Ogawa et al. [25] performed SSRT, fatigue life, fatigue crack growth (FCG) and fracture toughness tests on Cu-Be alloys (CDA-C17200) in high-pressure hydrogen gas, and demonstrated their excellent resistance to HE. The Cu-Be alloys exhibited a TS ranging from 1300 to 1400 MPa, which is the highest TS among materials with no degradation of tensile ductility that have been reported so far [24]. Wada et al. [26,27] investigated the effects of hydrogen on the SSRT properties of Cu-Ni alloys with varied Ni contents as a fundamental study on HE; as a result, the relative reduction in area (RRA) of the alloys increased with an increase in the Cu content, and the hydrogen-induced degradation of the RRA was mitigated at a Cu content of 70 wt.% or larger, although the TS did not reach a satisfactory level.

Although various studies have been conducted on materials with high resistance to HE, new highly HE-resistant materials satisfying both high TS and low cost have not yet been developed. In addition, if not only wrought and rolled alloys but also cast alloys were used for hydrogen components, they could be widely used. For example, research and development has recently been conducted on various hydrogen carriers such as liquid hydrogen in addition to high-pressure hydrogen, and

applications of larger-diameter valves have been investigated. In this context, the application of new cast alloys with excellent resistance to HE is a reasonable choice in consideration of machining processes and will help reduce the cost of hydrogen components. From this viewpoint, the present study focuses on highly HE-resistant cast alloys.

As a promising highly HE-resistant candidate, Cu-Al-Ni-Fe-Mn cast alloys (JIS H5120-CAC702 and CAC703, where JIS stands for Japanese Industrial Standards), referred to as aluminum bronze alloys, exhibit a higher TS than the nickel-equivalent material with a typical TS of 550 MPa [12] and Type 304 stainless steel with a typical TS of 620 MPa [12]. Since the Cu content of the alloys is 78 wt.% or larger, they are expected to have a high resistance to HE, according to the report by Wada et al. [26,27]. In fact, Michler et al. [28] reported that the tensile and fatigue life properties of Cu-Al-Ni-Fe wrought alloys were not degraded in 10 MPa hydrogen gas, although the tested gas pressure was lower than 100 MPa; therefore, the Cu-Al-Ni-Fe-Mn alloys (CAC702 and CAC703) are also expected to have excellent resistance to HE. Although the TS of the Cu-Al-Ni-Fe-Mn alloys is lower than that of the Cu-Be alloys, the Cu-Al-Ni-Fe-Mn alloys have lower cost than the Cu-Be alloys and moreover, contain no Be element which is poisonous. In addition, the alloys have a more advantage in machinability than austenitic stainless steels. Thus, if an excellent resistance to HE is demonstrated by the Cu-Al-Ni-Fe-Mn alloys, the alloys are expected to be actively used for hydrogen components.

The objective of the present study was to clarify the hydrogen compatibility of Cu-Al-Ni-Fe-Mn alloys in 100 MPa high-pressure gaseous hydrogen. According to existing literatures [29–31], the microstructures of the alloys were expected to significantly vary due to slight differences in their chemical compositions. Thus, four types of Cu-Al-Ni-Fe-Mn alloys were prepared with varying Al and Ni contents. These alloys were exposed to 100 MPa hydrogen gas, after which their hydrogen diffusion properties and hydrogen-induced ductility loss were investigated. SSRT tests were also conducted on some of the alloys in 100 MPa hydrogen gas and the hydrogen compatibility of the alloys was evaluated using both internal and external hydrogen.

2. Experimental procedure

2.1 Materials

The four types of Cu-Al-Ni-Fe-Mn cast alloys used in this study are denoted as Materials A through D. Material A is mass-produced and the other materials are prototypes; therefore, Material A is regarded as a base alloy. Ingots with a diameter of 25 mm and length of 200 mm as regulated in JIS-H5120 were manufactured via sand mold casting. The alloys were sampled from molten metals and the chemical composition of the alloys was analyzed by optical emission spectroscopy (OES). Material A consisted of 9.2 Al, 1.7 Ni, 3.6 Fe, and 1.0 Mn in wt.% and the balance was Cu (Cu-9.2 Al-1.7 Ni-3.6 Fe-1.0 Mn). In comparison, Materials B, C, and D had a larger amount of Al (Cu-10.3 Al-1.6 Ni-3.3

Fe-0.9 Mn), a larger amount of Ni (Cu-9.2 Al-3.9 Ni-3.6 Fe-0.9 Mn) and larger amounts of both Al and Ni (Cu-10.2 Al-3.8 Ni-3.8 Fe-1.0 Mn), respectively. The chemical composition of these alloys satisfied the following specifications of JIS-H5120: 80.0–88.0 Cu, 8.0–10.5 Al, 1.0–3.0 Ni, 2.5–5.0 Fe, 0.1–1.5 Mn and 0.7 others in CAC702; 78.0–85.0 Cu, 8.0–10.5 Al, 3.0–6.0 Ni, 3.0–6.0 Fe, 0.1–1.5 Mn and 0.7 others in CAC703. The main difference between CAC702 and CAC703 is the Ni content.

Regarding the tensile properties, the regulation requires TS of ≥490 MPa for CAC702 and elongation of ≥20%, while it requires TS of ≥590 MPa and elongation of ≥15% for CAC703. Namely, the required TS in the standard is higher for CAC 703 than for CAC702. Materials A and B belong to CAC702 and their Al contents were the middle value and near the upper limit of the specification, respectively. Materials C and D belong to CAC703 and their Al contents were the middle value and near the upper limit of the specification, respectively.

2.2 Specimens, hydrogen charging and microstructural analysis

Smooth, round bar specimens with a diameter of 6 mm and gage length of 30 mm were machined from the ingots in accordance with ASTM-E8M. After the turning process, the gage section was polished with emery papers, followed by alumina polishing pads. Cylindrical specimens with a diameter of 5 mm and length of 5 mm were cut from the ingot for measuring the hydrogen diffusion properties, after which all the surfaces were polished as well as the smooth, round bar specimens. Some of the specimens were exposed to 100 MPa hydrogen gas at a temperature of 270°C for 200 h. According to a past study on Cu-Ni alloys by Wada et al. [27], the hydrogen diffusivity at 270°C is estimated as 2×10^{-11} m^2/s at a minimum. The hydrogen diffusivity is denoted by D and the exposure time is denoted by t. If $\sqrt{Dt}$ is larger than the radius of a specimen, the specimen approximately reaches a uniform hydrogen distribution. When $D = 2\times10^{-11}$ m^2/s and t = 200 h, $\sqrt{Dt}$ is calculated as 3.8 mm. Since the value of $\sqrt{Dt}$ was larger than the specimen radii (3 mm for the SSRT specimen, 2.5 mm for the cylindrical specimen for determining the hydrogen diffusion properties), it can be interpreted that the hydrogen concentations in the SSRT and cylindrical specimens reached a uniform distribution under the present hydrogen exposure conditions.

Rationality of the D value is confirmed experimentally in the following section. The microstructures of the alloys were analyzed via scanning elecron microscopy (SEM) / energy dispersive X-ray spectroscopy (EDX). In addition, X-ray diffraction (XRD) was also used for structural analysis of some of the alloys. The X-ray detector was a two-dimensional imaging plate and the diameter of a collimator was 300 μm. To reduce the effect of the crystal orientation, angles of φ and ω were rotated at 1°/s and 2°/s (25°–35°) during 30 min, respectively.

2.3 Measurement of hydrogen content and diffusivity

Hydrogen contents and diffusivity were measured under a rising or constant temperature, using gas chromatography–mass spectroscopy (GC–MS). The saturated hydrogen contents in the specimens were determined by measurement under a rising temperature, known as thermal desorption analysis (TDA). The heating rate was 100°C/h and the evaluated temperature ranged from room temperature up to 800°C. Hydrogen diffusivity was determined by fitting the solution of a diffusion equation to the residual hydrogen contents measured at various constant temperatures [32–35].

$$C_{\mathrm{R}}(t_{\mathrm{R}}) = \frac{32}{\pi^2} \cdot A_{\mathrm{R}} \cdot \left\{ \sum_{n=0}^{\infty} \frac{\exp\left[-\frac{(2n+1)^2 \pi^2 D t_{\mathrm{R}}}{h^2} \right]}{(2n+1)^2} \right\} \cdot \left\{ \sum_{m=1}^{\infty} \frac{\exp\left[-\frac{D \beta_m^2 t_{\mathrm{R}}}{r^2} \right]}{\beta_m^2} \right\} + C_0 \quad (1)$$

where A_{R} is the coefficient related to the saturated hydrogen content, D is the hydrogen diffusivity, t_{R} is the holding time in GC–MS, β_{m} is the square root of the zero-order Bessel function, C_0 is the nondiffusible hydrogen content, h is the specimen length, and r is the specimen radius. Since the experimental data contained hydrogen contents during a rapid heating process before reaching a constant temperature, the fitting was performed by excluding the data during the process. Thus, the strict solution of Eq. (1) is not A_{R} but the saturated hydrogen content minus nondiffusible hydrogen contents, $C_{\mathrm{S}} - C_0$; however, the determined A_{R} value is not necessarily consistent with the value of $C_{\mathrm{S}} - C_0$.

2.4 SSRT test and observation of fracture surfaces

SSRT tests of uncharged and hydrogen-charged (H-charged) specimens were conducted at a displacement rate of 0.09 mm/min, which corresponds to a strain rate of 5×10^{-5} s^{-1}, in air at room temperature. For Material B, SSRT tests were also conducted at a displacement rate of 0.09 mm/min in 100 MPa hydrogen gas at room temperature. After the SSRT tests, the fracture surfaces were observed via SEM.

3. Experimental results

3.1 Microstructural characterization

Since microstructures of the Cu-Al-Ni-Fe-Mn alloys are complex, some phase diagrams are firstly indicated in **Fig. 1(a)** [36.37]. The microstructures of the Cu-Al-Ni-Fe alloys at room temperature were thoroughly investigated by Kanamori et al. [38] and its maps are shown in **Fig. 1(b)**, toghter with the expected microstructures of Materials A–D. Following the investigations, it is expected that Materials A, B and D consist of α, γ_2, and κ, while Material C consists of α and κ. The α phase is a Cu solid solution containing Al, which is referred to as the α-solid solution. The γ_2 phase is based on Cu_9Al_4, which is formed by a eutectoid reaction. The κ precipitate is recognized as FeAl (or Fe_3Al) corresponding to Fe-

rich precipitates or NiAl corresponding to Ni-rich precipitates, which is generally classified into the following five types [30]:

κ_{I} : Fe rich, primary precipitate from melt

κ_{II} : Fe rich, precipitate from β phase

κ_{III} : Ni rich, part of eutectoid structure $\alpha + \kappa_{III}$

κ_{IV} : Fe rich, globular precipitate from α phase

κ_{V} : Fe rich, lath precipitate from α phase

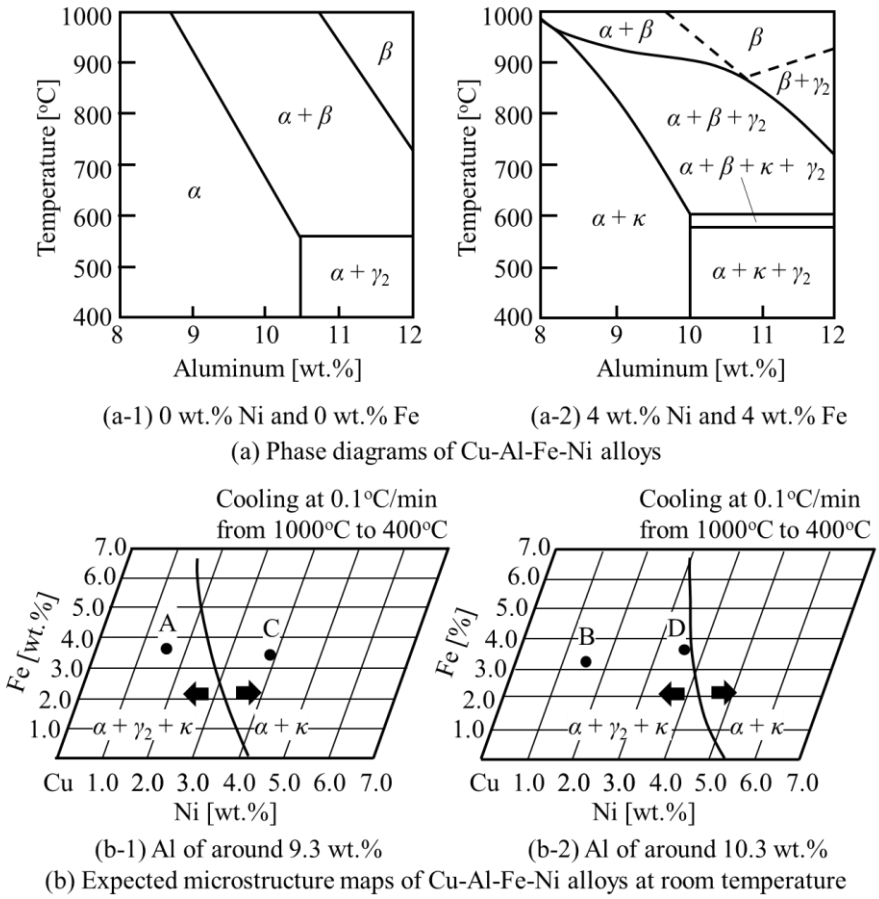

(a-1) 0 wt.% Ni and 0 wt.% Fe (a-2) 4 wt.% Ni and 4 wt.% Fe

(a) Phase diagrams of Cu-Al-Fe-Ni alloys

(b-1) Al of around 9.3 wt.% (b-2) Al of around 10.3 wt.%

(b) Expected microstructure maps of Cu-Al-Fe-Ni alloys at room temperature

Fig. 1. Phase diagrams and expected microstructure maps of Cu-Al-Ne-Fe alloys [36–38].

Figure 2 shows low magnification backscattered electron (BSE) images for the initial microstructures of Materials A–D. While the matrix structures of Materials A and C had equiaxial grains with an average size of around 30 μm, those of Materials B and D in which a larger amount of Al was added compared with that of Material A had fine, elongated grains. The grain sorrounded by a broken, red line shown in **Fig. 2(a)** is an example of eutectoid structures. Although the details will be mentioned later, while the matrix structures of Matearials A and B were composed of the α-solid

solutions and the eutectoid structures, the matrix structures of Materials C and D were composed of only the α-solid solutions and neglibile eutectoid structures were observed.

Figure 3 shows results of structural analyses of Materials B and C by XRD. The experimental spectra were reconstructed by superposing the spectra for $Cu_{0.85}Al_{0.15}$, $Cu_{2.74}Ni_{0.15}Al_{1.11}$ and NiAl. Although it is difficult to confirm the existence of Fe-rich precipitates such as FeAl and Fe_3Al due to overlaps of various X-ray peaks, the existences of $Cu_{0.85}Al_{0.15}$, $Cu_{2.74}Ni_{0.15}Al_{1.11}$ and NiAl were at least confirmed. While $Cu_{0.85}Al_{0.15}$ and $Cu_{2.74}Ni_{0.15}Al_{1.11}$ were detcted in Materials B and C, NiAl was detected in only Material C. $Cu_{0.85}Al_{0.15}$, $Cu_{2.74}Ni_{0.15}Al_{1.11}$ and NiAl were interpreted as the α-solid solution, the γ_2 phase and the κ_{III} precipitate, respectively.

Figures 4 and **5** show high magnification BSE and element mapping images for the initial microsctures of Materials B and C analyzed by SEM/EDX. White areas were observed in the matrix structures in Material B, while such white areas were not hardly detected in Material C. Compostions of the matrix structures with and without the white areas were measured at ten points via the ZAF correlation method in consideration of Cu and Al under a spatial resolution of 2 μm. The matrix structures without the white areas had 19.63 at.% Al–80.37 at.% Cu with a standard deviation of 0.69 for Material B and 20.87 at.% Al–79.13 at.% Cu for Material C with a standard deviation of 1.73, repectively. Although these atomic ratios of Al were slightly higer than the ratio determined by the XRD analyses ($Cu_{0.85}Al_{0.15}$), this difference is speculated to be attributed to fine Fe- and Ni-rich precipitates

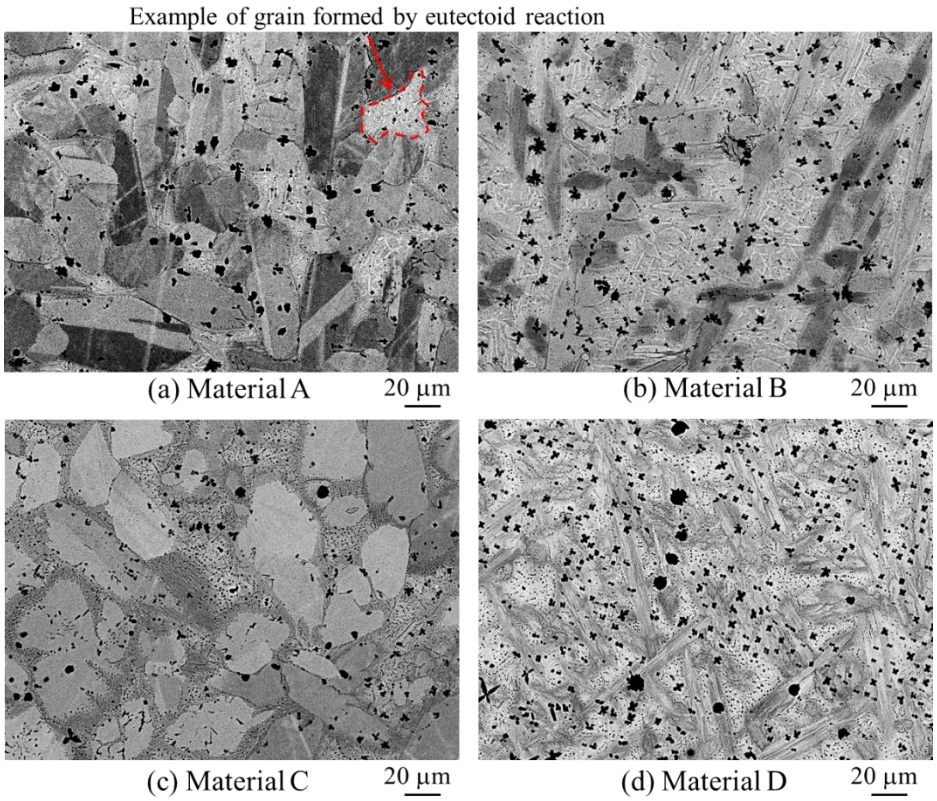

Fig. 2. BSE images of intitial microstructures of Materials A–D under low magnification.

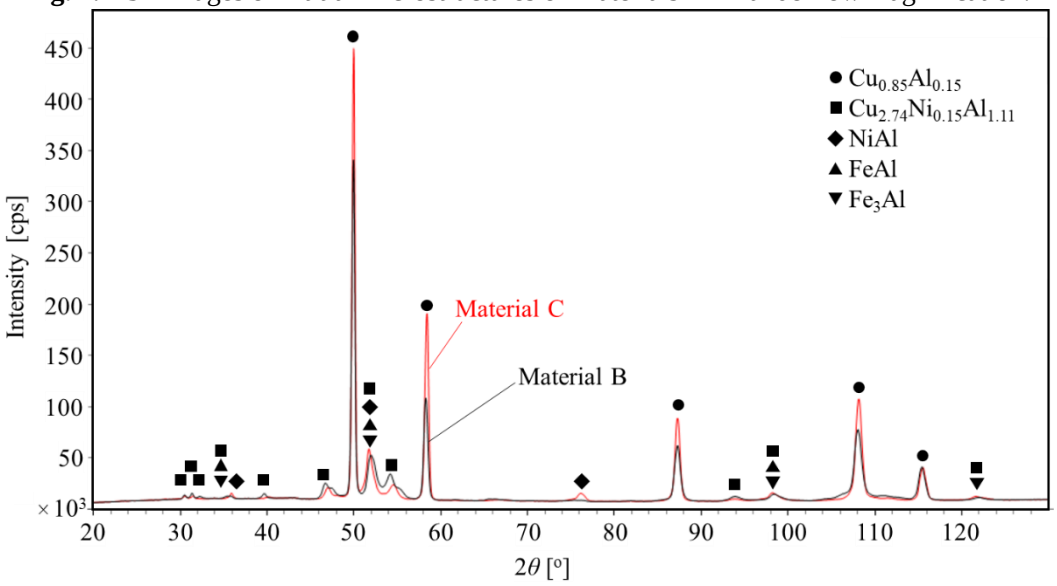

Fig. 3 X-ray diffraction patterns for Materials B and C via XRD.

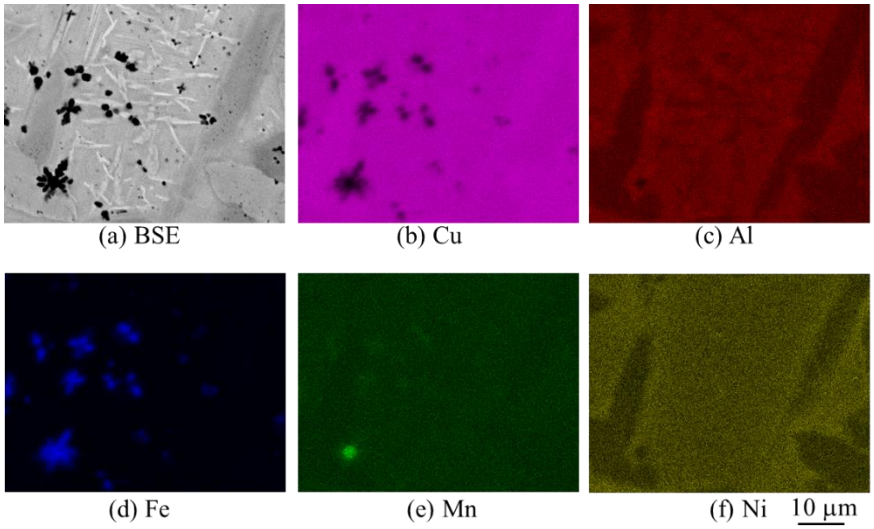

Fig. 4. SEM/EDX images of intitial microstructures of Material B under high magnification.

in the α-solid solutions. Hence, the compositions determined from the SEM/EDX analyses corresponded with $Cu_{0.85}Al_{0.15}$ in the XRD analyses and these structures were identified as the α-solid solutions.

In constrast, the matrix structure with the white areas had 26.52 at.% Al–73.48 at.% Cu with a standard deviation of 1.17 for Material B. This compostion could be interpreted to correpond with a mixture of the α-solid solutions and the γ_2 phases; therefore, the matrix structure with the white areas was identified as the eutectoid structure. The eutectoid structures were detected in Materials A and B, the area fractions of which were 11% in Material A and 37% in Material B from the BSE image in **Fig.**

2. Although X-ray peaks corresponding to the γ_2 phases were detected from Material C as well as Material B, the obvious eutectoid grains were not detected from the BSE image of Material C in **Fig. 2**.

Regarding κ precipitates, according to the XRD and SEM/EDX analyses in **Figs. 3** to **5**, while only Fe-rich precipitates were detected in Material B, both Fe- and Ni-rich precipitates were detected in Material C, revealing that the dispersion of κ precipitates differed between the alloys. **Figure 6** shows high magnification BSE and Ni element mapping images for the initial microsctures of Materials A–D analyzed by SEM/EDX. The κ_{III} precipitates corresponding with the Ni-rich ones were detected in Materials C and D with negligible eutectoid structures. Since β is decomposed into either α and γ_2 or α and κ_{III} precipitates during the cooling process, the ratio of κ_{III} precipitates becomes lower at a higher ratio of γ_2 and conversely, the ratio of κ_{III} precipitates becomes higher at a lower ratio of γ_2. Therefore, it follows that the alloy with a higher ratio of γ_2 such as Material B showed a lower ratio of κ_{III} precipitates, while the alloy with a lower ratio of γ_2 such as Material C showed a higher ratio of κ_{III} precipitates.

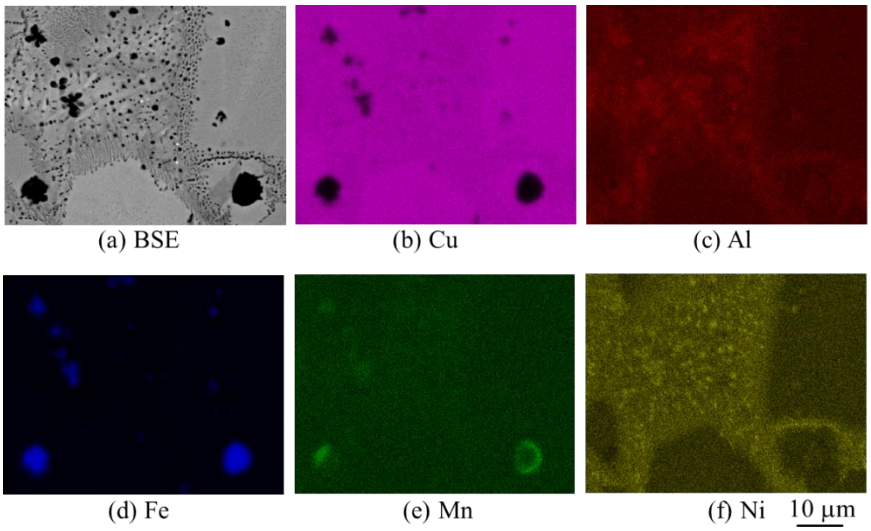

Fig. 5 SEM/EDX images of intitial microstructures of Material C under high magnification.

3.2 Hydrogen uptake after exposure to high-pressure hydrogen gas

Figure 7 shows the TDA profiles of uncharged and H-charged specimens of Materials A–D. Peaks appeared at around 450–500°C for the uncharged and H-charged specimens of all the alloys. Although the hydrogen desorption rate dropped once and had a local minimum at around 600°C, the rate gradually increased at temperatures higher than 600°C. The hydrogen content ranged from 1.72 to 2.77 wt.ppm and was never zero even in the uncharged specimens. The hydrogen detected from the uncharged specimens is deemed to be absorbed during the casting process. On the other hand, the hydrogen content of the H-charged specimens ranged from 2.65 to 4.49 wt.ppm. The hydrogen uptakes after exposure (in wt.ppm) of the alloys were 0.93 (Material A), 1.48 (Material B), 1.72 (Material C),

and 1.46 (Material D). Although the hydrogen uptake depended on the alloy, it was in the order of 1 wt.ppm, which is nearly equal to that of pure Cu [27]. The smallest hydrogen uptake was in Material A, which was increased by adding Al and/or Ni. Material C with a larger amount of Ni had the highest content. Although the hydrogen uptake of Material C was approximately twice larger than that of Material A, it was considerably smaller than that of austenitic stainless steel (around 100 wt.ppm [12]) under the same hydrogen exposure conditions.

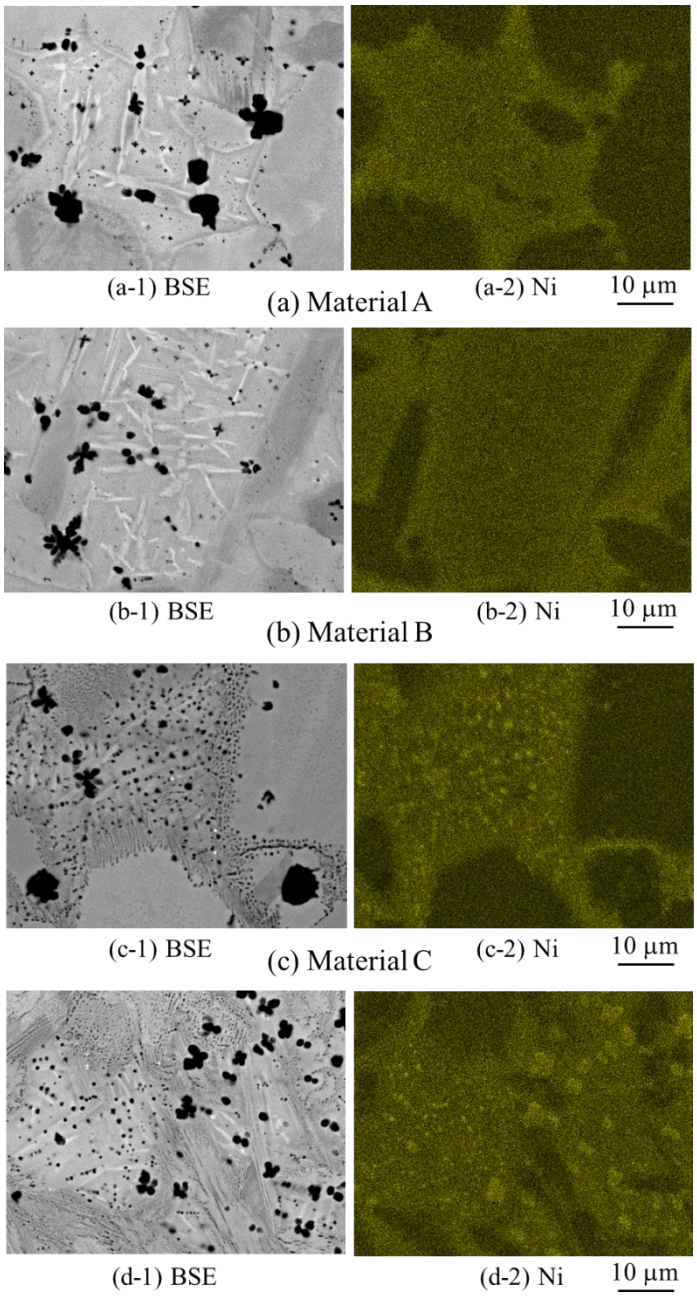

Fig. 6. BSE and Ni element mapping images of intitial microstructures of Materials A–D under high magnification.

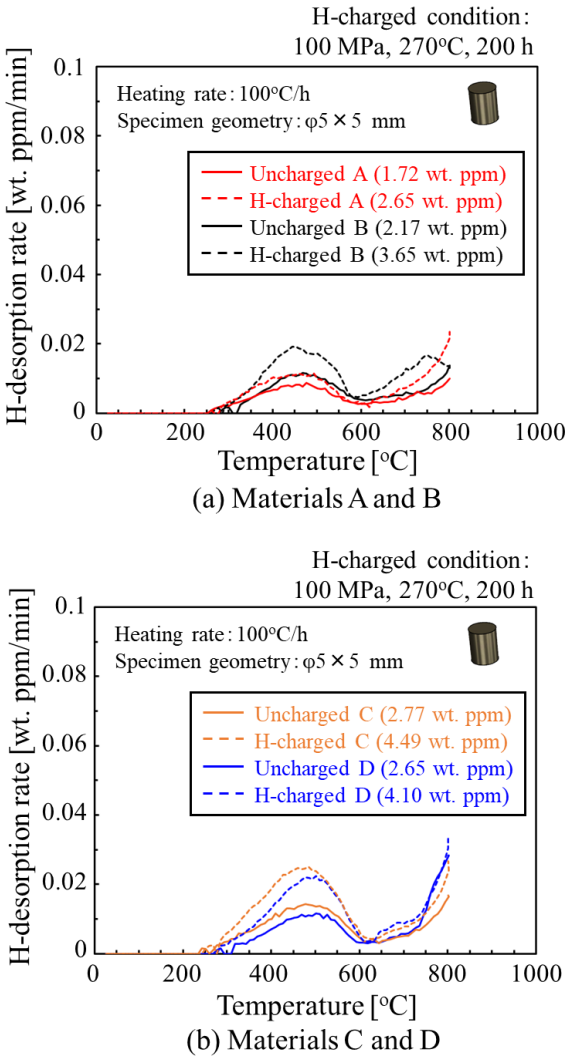

Fig. 7. TDA profiles of uncharged and H-charged specimens of Materials A–D.

3.3 Hydrogen diffusivity

Figure 8 shows the hydrogen desorption behavior of a H-charged specimen of Material D at a constant temperature of 400°C. A fitted curve by Eq. (1) is also provided in this figure. The experimental data were successfully fitted by Eq. (1) and the coefficient of determination, R^2, was 0.99. In this case, the determined hydrogen diffusivity, D, was 1.06×10^{-10} m^2/s.

Figure 9 shows the Arrhenius plots of the determined hydrogen diffusivity of Materials A–D together with literature data [27,38]. The data provided the hydrogen diffusivities of pure Cu, pure Ni, and Cu-Ni alloy. According to the data, the hydrogen diffusivity of pure Cu was smaller than that of pure Ni and the hydrogen diffusivity of Cu-Ni alloys was dependent on the ratio of Cu and Ni, being lowest at a Ni content of 30 wt.%. Regarding Materials A–D, the hydrogen diffusivity of Material A with the smallest hydrogen uptake was slightly larger than that of the other materials. However, there

was no substantial difference between these values, which were nearly equal to that of Cu-30%Ni

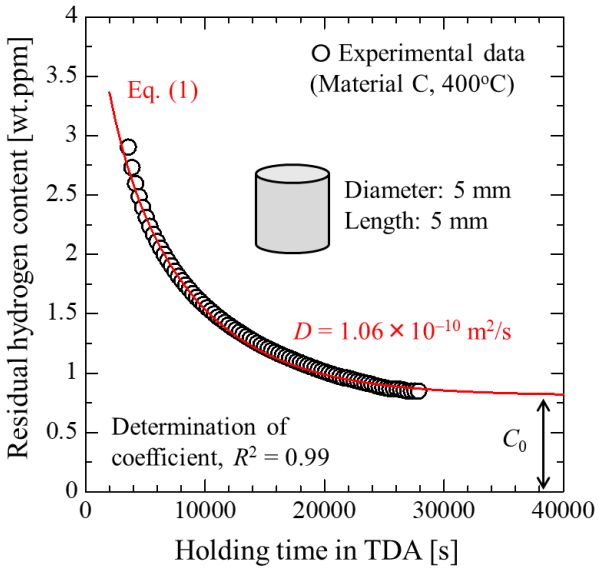

Fig. 8. Relationship between residual hydrogen content and holding time in TDA of Material C under a constant temperature of 400°C. The coefficient of determination, R^2, was 0.99.

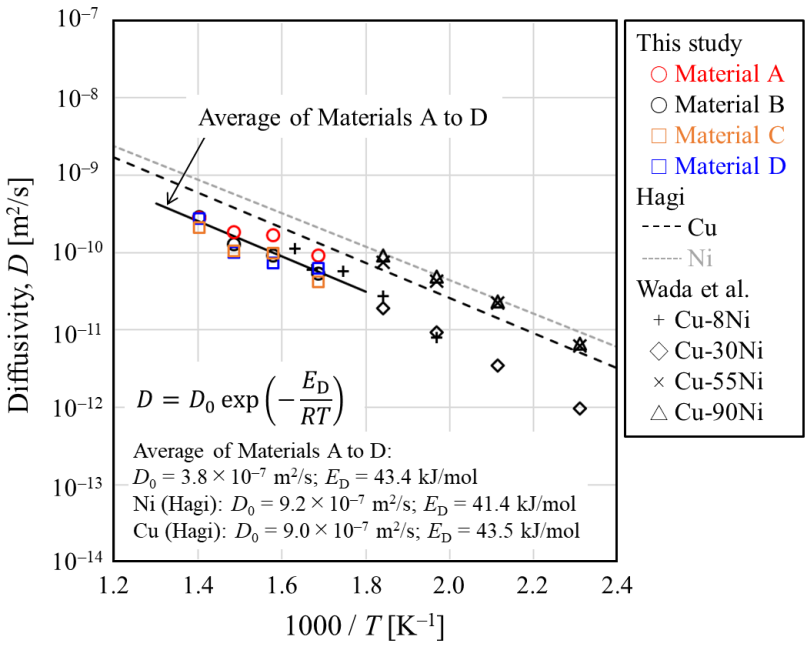

Fig. 9. Temperature dependence of hydrogen diffusivity of Materials A–D together with literature data by Hagi [38] and Wada et al. [27].

reported by Wada et al. [27]. The average activation energy of the hydrogen diffusivity, E_D, of Materials A–D was 43.5 kJ/mol, which is consistent with that of pure Cu reported by Hagi [38]. Although the hydrogen exposure conditions in the present study were calculated from the hydrogen

diffusivity of Cu-30%Ni, not Materials A–D, the hydrogen diffusivity of Cu-30Ni was nearly equal to that of Materials A–D; thus, it was confirmed that the present hydrogen exposure conditions were reasonable for obtaining a uniform hydrogen concentration.

SSRT tests of H-charged pure Ni and Cu-Ni alloys with similar hydrogen diffusivity to Materials A–D were conducted under the same experimental condition and their hydrogen-induced ductility losses have been confirmed [27]. This asserts that the hydrogen compatibility of Materials A–D can be also evaluated under the present experimental condition with internal hydrogen.

3.4 Tensile properties with internal hydrogen

Figure 10 shows the SSRT test results for the uncharged and H-charged specimens of Materials A–D. The values of the TS, reduction in area (RA), relative TS (RTS), and relative RA (RRA) are also provided in the figure. When comparing the TS of the uncharged specimens, that of Material A was 638 MPa, which was higher than the typical TS values of the nickel-equivalent material (550 MPa) and Type 304 (620 MPa). Material D with larger amounts of both Al and Ni had the maximum TS (757 MPa), which was 1.4 times higher than that of the nickel-equivalent material. The TS of Material B with a larger amount of Al and that of Material C with a larger amount of Ni were 651 and 644 MPa, respectively, and both were slightly higher than that of Material A. Regarding tensile ductility, the RAs of Materials B and D were lower than those of Materials A and C, revealing that the larger amount of Al remarkably degraded the ductility. On the other hand, the tensile ductility of Material C with a larger amount of Ni was nearly equal to that of Material A and therefore, the larger amount of Ni did not affect the ductility.

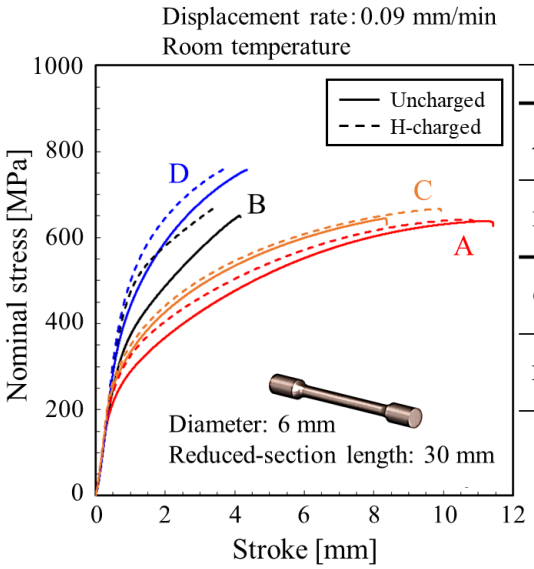

Material		TS [MPa]	RA	RTS	RRA
A	H-charged	641	0.26	1.01	1.00
	Uncharged	638	0.26		
B	H-charged	668	0.09	1.03	1.00
	Uncharged	651	0.09		
C	H-charged	667	0.24	1.04	1.26
	Uncharged	644	0.19		
D	H-charged	759	0.10	1.01	1.00
	Uncharged	757	0.10		

TS: tensile strength; RA: reduction in area;
RTS: relative TS; RRA: relative RA

Fig. 10. SSRT test results of Materials A–D with internal hydrogen.

As for the effects of hydrogen on tensile ductility, the values of RTS and RRA of Materials A–D were 1 or higher, although the tensile ductility of pure Ni and Cu-Ni alloys were significantly degraded under the present H-charged condition. The microstructures were not the same among the alloys; however, the tensile ductility of all the alloys was not degraded by internal hydrogen.

In addition, flow stresses of Materials A–D were improved. The increase in the flow stresses by hydrogen charging was also observed from Ni and Cu-Ni alloy in our previous study [26]. Although this study does not discuss this hardening behavior, the previous study concludes that the hardening effect of hydrogen can be explained by a combination of enhanced evolution of dislocation structure and solid-solution strengthening.

3.5 Fracture surface morphologies

Figures 11(a) and **(b)** display the fracture surface morphologies for uncharged and H-charged specimens of Materials A and B, respectively. The uncharged specimens of Materials A and B showed the same fracture surface morphologies as the H-charged specimens, revealing the absence of hydrogen effects on the fracture surface morphologies. Flat facets (a) with sizes of several tens of microns and dimples (b) were observed on the fracture surfaces of both Materials A and B, although the morphology of the matrix structure of Material A differed from that of Material B. This verifies that the flat surfaces are not related to a difference in the morphology of their matrix structures. These flat surfaces were not detected in Materials C and D with a negligible ratio of γ_2 phases, as shown in **Fig. 12** later, which suggests that the flat surfaces are attributed to fractures related to the γ_2 phases.

Figures 12(a) and **(b)** display the fracture surface morphologies for uncharged and H-charged specimens of Materials C and D, respectively. As with Materials A and B, the uncharged specimens of Materials C and D showed the same fracture surface morphologies as the H-charged specimens; therefore, the effects of hydrogen on the fracture surface morphologies were also negligible. However, the fracture surfaces of both Materials C and D were mainly covered with fine dimples, which differed from those of Materials A and B. Since Materials C and D had κ_{III} precipitates with sizes of several microns, these precipitates were presumed to be the origins of void formations.

In addition, as shown in **Fig. 12(a-3)**, a relatively large casting defect with a size of around 200 μm was observed on the fracture surface of the uncharged specimen of Material C (**Fig. 12(a-3)**). This casting defect reduced the RA of the uncharged specimen (RA = 0.19) compared to the H-charged specimen (RA = 0.24) and consequently, the RRA of Material C was deemed to be 1.26. This may indicate that the alloys other than Material A were prototypes and further developments of the alloys are needed.

A series of hydrogen compatibility evaluations with internal hydrogen demonstrated that hydrogen-induced ductility loss did not occur in Materials A to D and that HE resistance was excellent

in the Cu-Al-Ni-Fe-Mn cast alloys. The following section presents an overview of the SSRT tests conducted on Material A in 100 MPa hydrogen gas on behalf of Materials A–D.

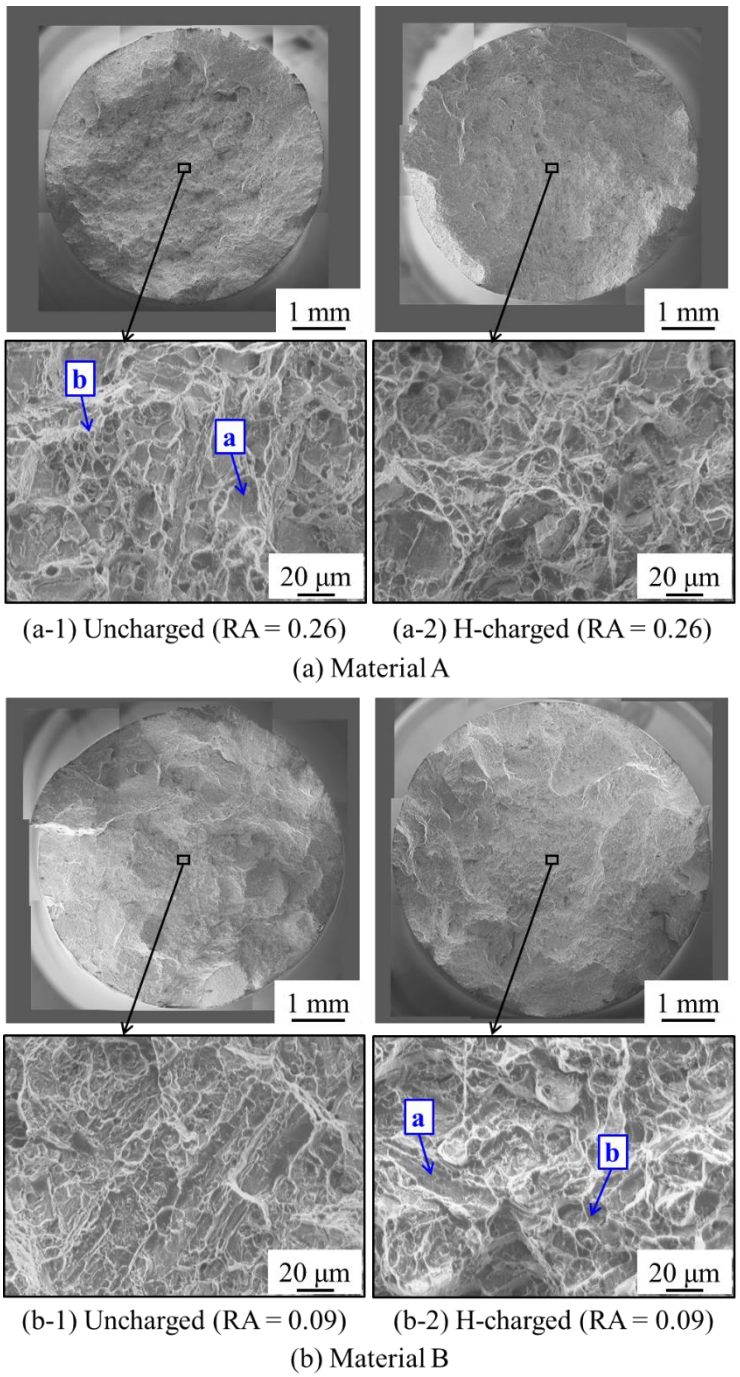

Fig. 11. Fracture surface morphologies for uncharged and H-charged specimens of Materials A and B via SEM. a and b are flat surfaces and dimples, respectively.

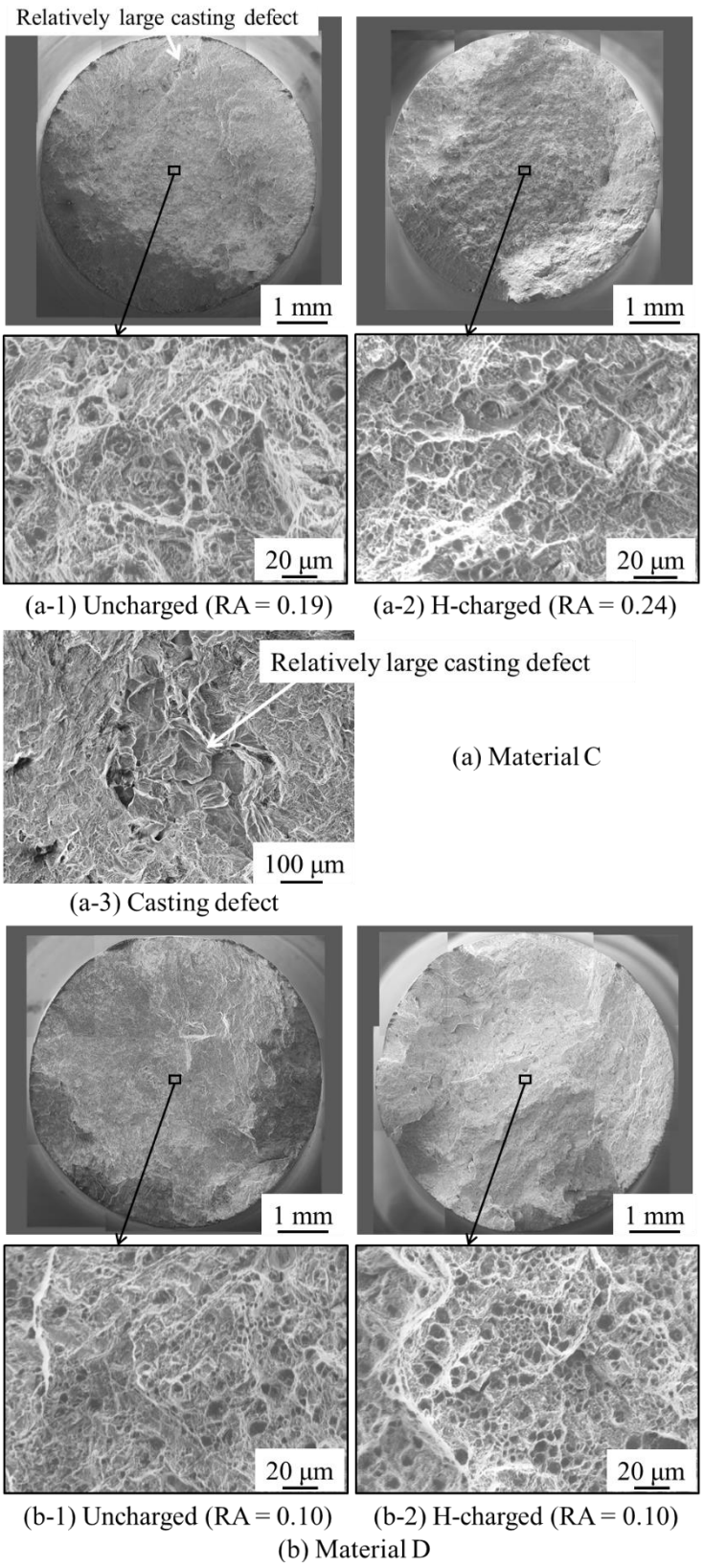

Fig. 12. Fracture surface morphologies for uncharged and H-charged specimens of Materials C and D via SEM.

3.6 Tensile properties and fracture surface morphologies of Material A in external hydrogen

SSRT tests were performed on Material A in 100 MPa hydrogen gas at room temperature. **Figure 13(a)**, **(b)**, and **(c)** show the SSRT test results, optical microscopy images of fractured specimens, and fracture surface morphologies, respectively. In addition to RRA ≈ 1, the specimens tested in air and hydrogen gas showed similar fracture surface morphologies. These results demonstrated that there was no tensile ductility loss due to external hydrogen.

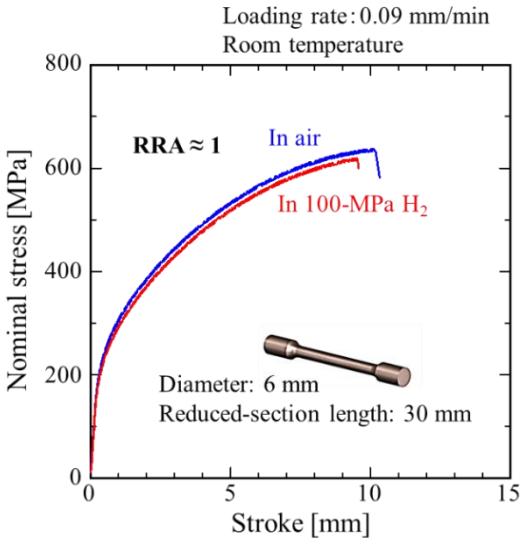

(a) Nominal stress and stoke curves

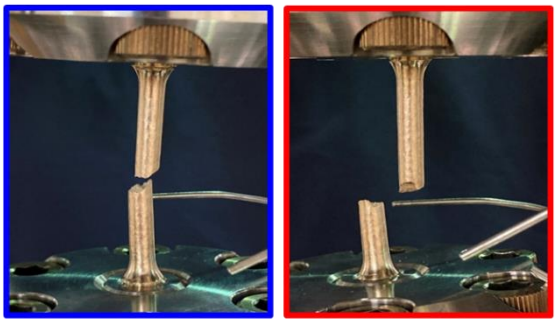

(b-1) In air (b-2) 100-MPa H_2

(b) Fractured specimens

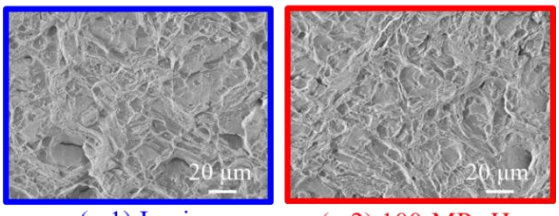

(c-1) In air (c-2) 100-MPa H_2

(c) Fractur-surface morphologies

Fig. 13. SSRT properties and fracture morphologies of Material A in external hydrogen.

4 Discussion

4.1 Effect of microstructure on hydrogen uptake and hydrogen diffusivity

Table 1 summarizes the microstructures, hydrogen uptakes, hydrogen diffusivity, tensile properties (TS and RA), and fracture surface morphologies of Materials A–D. The matrix structure of Material A consisted of α-solid solutions and eutectoid structures with equiaxial grains containing κ precipitates. The matrix structure of Material B consisted of α-solid solutions and eutectoid structures with fine, elongated grains containing κ precipitates. The matrix structure of Material C consisted of α-solid solutions with equiaxial grains containing κ precipitates and then, κ_{III} precipitates and negligible eutectoid structures were observed, different from Materials A and B. The matrix structure of Material D consisted of α-solid solutions with fine, elongated grains containing κ precipitates; then, κ_{III} precipitates and negligible eutectoid structures were observed as well as Material C. As described above, although the chemical composition of Materials A–D satisfied the JIS specifications, the materials showed very different microstructures. In this context, the relationship between the microstructures, hydrogen uptake, and tensile properties are discussed.

The relationship between the microstructures and hydrogen uptakes is discussed first. Among Materials A–D, the hydrogen uptake of Material A was the smallest. In contrast, Material C showed the largest hydrogen uptake, although Materials A and C had similar matrix structures. Thus, the elevated hydrogen uptake was interpreted to be mainly attributed to hydrogen trapping rather than different matrix structures, although the matrix structures might somewhat affect the hydrogen uptake. The reason why Material A showed the smallest hydrogen uptake was deemed to be because of a lower number of hydrogen-trapping sites than the other alloys. The ratio of the γ_2 phases was higher in Material B than in Material A, while that of κ precipitates in Materials C and D was higher than that in Material A. It can be interpreted that multiple hydrogen trapping effects by both the γ_2 phases and κ precipitates contributed to the larger hydrogen uptakes of Materials B–D, compared to Material A.

Regarding the hydrogen diffusivity of Materials A–D, the hydrogen diffusivity of Materials B–D was slightly lower than that of Material A. While the ratio of the γ_2 phases was higher in Material B than in Material A, the ratio of κ precipitates in Materials C and D was higher than that in Material A. Thus, it is deemed that hydrogen trapped by γ_2 phases and/or κ precipitates contributed to hydrogen diffusion, causing a slight decrease in the hydrogen diffusivity of Materials B–D, compared with that of Material A.

4.2 Effect of microstructure on tensile properties

The relationship between the microstructures and tensile properties is then discussed. The α-solid solution with fine, elongated grains contributed to the improvement of TS, although it significantly degraded the RA. The difference in the morphology of the matrix structures is attributed to the formation rates of the α-solid solutions by the varied Al contents. It is presumed that

strengthening mechanisms such as grain refinement and solid-solution strengthening were activated in the case of α-solid solutions with fine, elongated grains; consequently, its matrix structure showed higher deformation resistance than α-solid solutions with equiaxial grains. Regarding the effect of the γ_2 phases and κ precipitates on the tensile properties, the TS was improved when the ratio of the γ_2 phases became lower and that of the κ precipitates became higher, although the RA hardly changed. This is considered to be because the γ_2 phases were brittle and degraded the tensile properties, while the κ precipitates enhanced the tensile ductility by dispersion strengthening.

Table 1 Summary of microstructure, hydrogen uptake, TS, RA, and fracture surface morphology

Material	Chemical composition	Microstructure	H-uptake [wt.ppm]	H-diffusivity at 400ºC [m^2/s]	TS [MPa]*	RA*	Fracture surfaces morphology
A	Cu-9.2Al-1.7Ni-3.6Fe-1.0Mn	・α-solid solutions and eutectoid structures with equiaxial grains containing κ precipitates ・Area fraction of eutectoid structures with 37%	0.93	1.82×10^{-10}	638 (U) 641 (H)	0.26 (U) 0.26 (H)	Dimples and flat surfaces
B	Cu-10.3Al-1.6Ni-3.3Fe-0.9Mn	・α-solid solutions and eutectoid structures with fine, elongated grains containing κ precipitates ・Area fraction of eutectoid structures with 11%	1.48	1.27×10^{-10}	651 (U) 668 (H)	0.09 (U) 0.09 (H)	Dimples and flat surfaces
C	Cu-9.2Al-3.9Ni-3.6Fe-0.9Mn	・α-solid solutions with equiaxial grains containing κ precipitates ・Many κ_{III} precipitates ・Negligible area fraction of eutectoid structures	1.76	1.06×10^{-10}	644 (U) 667 (H)	0.19 (U) 0.24 (H)	Fine dimples
D	Cu-10.2Al-3.8Ni-3.8Fe-1.0Mn	・α-solid solutions with fine, elongated grains containing κ precipitates ・Many κ_{III} precipitates ・Negligible area fraction of eutectoid structures	1.46	1.01×10^{-10}	757 (U) 759 (H)	0.10 (U) 0.10 (H)	Fine dimples

* U: Uncharged; H: H-charged

In the present study, Material A was the base alloy, and four types of Cu-Al-Ni-Fe-Mn cast alloys (Materials A–D) were prepared by varying the Al and Ni contents within the specifications documented in JIS-H5120 (CAC702 and CAC703). The hydrogen diffusion and HE properties of the

alloys were investigated and all the alloys showed excellent resistance to HE. On the other hand, the microstructures differed between the alloys, which remarkably affected the tensile properties. The alloy with a larger amount of both Al and Ni compared with Material A showed the highest TS within this study and a TS value of around 750 MPa could be realized. However, the elevated Al content significantly reduced the RA. Since the fractures of the alloys occurred during uniform deformation before necking, the elongation, EL, could be expressed under the constant-volume assumption during plastic deformation as follows:

$$\mathrm{EL} = \frac{1}{1 - \mathrm{RA}} - 1$$

The JIS specification requires the EL of ≥20% for CAC702 and ≥15% for CAC703; therefore, the corresponding RA values are ≥0.17 for CAC702 and ≥0.13 for CAC703, respectively. Since this study does not investigate the role of Fe and Mn to the tensile ductility of CAC702 and CAC703, it will be necessary to correctly understand the role of each alloying element to the tensile properties and optimize the chemical composition to ensure a compatible TS and RA.

4. Conclusion

This study determined hydrogen compatibility of Cu-Al-Ni-Fe-Mn cast alloys by investigating the effect of microstructures on the hydrogen diffusion properties and hydrogen-induced ductility losses of four types of the alloys (Materials A–D): Material A (Cu-9.2%Al-1.7%Ni-3.6%Fe-1.0%Mn) as the base alloy, Material B (Cu-10.3%Al-1.6%Ni-3.3%Fe-0.9%Mn) with a larger amount of Al, Material C (Cu-9.2%Al-3.9%Ni-3.6%Fe-0.9%Mn) with a larger amount of Ni, and Material D (Cu-10.2%Al-3.8%Ni-3.8%Fe-1.0%Mn) with larger amounts of both Al and Ni were prepared. SSRT tests were conducted on hydrogen-charged specimens of Materials A–D in air at room temperature and with uncharged specimens (Material A) in 100 MPa hydrogen gas at room temperature. Hydrogen diffusion properties of the alloys were also investigated with hydrogen-charged specimens of Materials A–D. The hydrogen-charged specimens were exposed to 100 MPa hydrogen gas at a temperature of 270°C for 200 h. The following conclusions were obtained:

1. While Materials A and C had equiaxial grains, those of Materials B and D had fine, elongated grains. The addition of a larger amount of Al facilitated the formation of the fine, elongated grains.
2. The matrix structures of Materials A and B consisted of α-solid solutions and eutectoid structures containing κ precipitates; however, the matrix structures of Materials C and D consisted of only α-solid solutions containing κ precipitates; then, negligible eutectoid structures were observed. κ_{III} precipitates were also detected in Materials C and D. The addition of a larger amount of Ni

decreased the γ_2 phases and increased the κ_{III} precipitates.

3. Although the hydrogen contents of Materials A–D were significantly lower than that of austenitic stainless steels under the same hydrogen-charging conditions, the hydrogen content of Material A was only slightly smaller than that of the other alloys. Material B had a higher ratio of γ_2 phases than Material A. Although the ratio of γ_2 phases of Materials C and D was lower than that of Material A, Materials C and D had a higher ratio of κ precipitates than Material A. Combined hydrogen trapping effects by the γ_2 phases and κ precipitates were deemed to be attributed to the larger hydrogen contents of Materials B–D than that of Material A.
4. Hydrogen diffusivity of Material A with the smallest hydrogen content was slightly lower than that of the other alloys; however, there was no significant difference in their values. The activation energy of the hydrogen diffusivity of the alloys was nearly equal to that of pure Cu.
5. The RRA of all the alloys was 1 or higher despite the different microstructures. The Cu-Al-Ni-Fe-Mn alloy had a higher TS than the nickel-equivalent materials and Type 304 stainless steel, showing excellent resistance to HE.
6. The α-solid solutions with fine, elongated grains by adding a larger amount of Al improved the TS and reduced the RA. On the other hand, the decrease in the γ_2 phases and the increase in the κ precipitates by adding a larger amount of Ni improved the TS without reducing the RA. The tensile properties were closely related to the microstructures, and the alloys had the maximum TS with larger amounts of both Al and Ni.

References

[1] Han G, He J, Fukuyama S, Yokogawa K. Effect of strain-induced martensite on hydrogen environment embrittlement of sensitized austenitic stainless steels at low temperature. Acta Metall 1998;46:4559–70. https://doi.org/10.1016/S1359-6454(98)00136-0

[2] Fukuyama S, Sun D, Zhang L, Wen M, Yokokawa K. Effect of temperature on hydrogen environment embrittlement of type 316 series austenitic stainless steels at low temperature. J Jpn Inst Met 2003;9:456–9. https://doi.org/10.2320/jinstmet1952.67.9_456

[3] San Marchi C, Somerday BP, Tang X, Schiroky GH. Effects of alloy composition and strain hardening on tensile fracture of hydrogen-precharged type 316 stainless steels. Int J Hydrogen Energy 2008;33:889–904. https://doi.org/10.1016/j.ijhydene.2007.10.046

[4] Michler T, Nauman J. Hydrogen environment embrittlement of austenitic stainless steels at low temperature. Int J Hydrogen Energy 2008;33:2111–22. https://doi.org/10.1016/j.ijhydene.2008.02.021

[5] Michler T, Yukhimchuk AA, Naumann J. Hydrogen environment embrittlement testing at low temperatures and high pressures. Corros Sci 2008;50:3519–26. https://doi.org/10.1016/j.corsci.2008.09.025

[6] San Marchi C, Michler T, Nibur KA, Somerday BP. On the physical differences between tensile testing of type 304 and 316 austenitic stainless steels with internal hydrogen and in external hydrogen. Int J Hydrogen Energy 2010;35:9736–45. https://doi.org/10.1016/j.ijhydene.2010.06.018

[7] Mine Y, Kimoto T. Hydrogen uptake in austenitic stainless steels by exposure to gaseous hydrogen and its effect on tensile deformation. Corros Sci 2011;53:2619–29. https://doi.org/10.1016/j.corsci.2011.04.022

[8] Michler T, San Marchi C, Naumann J, Weber S. Hydrogen environment embrittlement of stable austenitic steels. Int J Hydrogen Energy 2012;37:6231–46. https://doi.org/10.1016/j.ijhydene.2012.08.071

[9] Yamabe J, Matsuoka S, Murakami Y. Surface coating with a high resistance to hydrogen entry under high-pressure hydrogen-gas environment. Int J Hydrogen Energy 2013;38:10141–54. https://doi.org/10.1016/j.ijhydene.2013.05.152

[10] Matsuo T, Yamabe J, Matsuoka S. Effects of hydrogen on tensile properties and fracture surface morphologies of Type 316L stainless steel. Int J Hydrogen Energy 2014;39:3542–51. https://doi.org/10.1016/j.ijhydene.2013.12.099

[11] Matsuoka S, Yamabe J, Matsunaga H. Criteria for determining hydrogen compatibility and the mechanisms for hydrogen-assisted surface crack growth in austenitic stainless steels. Eng Fract Mech 2016;153:103–27. https://doi.org/10.1016/j.engfracmech.2015.12.023

[12] Yamabe J, Takakuwa O, Matsunaga H, Itoga H, Matsuoka S. Hydrogen diffusivity and tensile-ductility loss of solution-treated austenitic stainless steels with external and internal hydrogen. Int J Hydrogen Energy 42;2017:13289–99. https://doi.org/10.1016/j.ijhydene.2017.04.055

[13] Takakuwa O, Yamabe J, Matsunaga H, Matsuoka S. Comprehensive understanding of ductility loss mechanisms in various steels with external and internal hydrogen. Metall Mater Trans A 2017;48:5717–32. https://doi.org/10.1007/s11661-017-4323-3

[14] Kobayashi H, Yamada T, Kobayashi H, Matsuoka S. Criteria for selecting materials to be used for hydrogen refueling station equipment. ASME PVP2016-64033; 2016. https://doi.org/10.1115/PVP2016-64033

[15] Hirayama T, Ogirima M. Influence of chemical composition on martensitic transformation in Fe-Cr-Ni stainless steel. J Jpn Inst Met 1970;34:507–10. https://doi.org/10.2320/jinstmet1952.34.5_507

[16] Takaki S, Namba S, Imakawa K, Macadre A, Yamabe J, Matsunaga H, Matsuoka S. Determination of hydrogen compatibility for solution-treated austenitic stainless steels based on a newly proposed nickel-equivalent equation. Int J Hydrogen Energy 2016;41:15095–100. https://doi.org/10.1016/j.ijhydene.2016.06.193

[17] San Marchi C, Somerday BP, Nibur KA. Development of Methods for Evaluating Hydrogen Compatibility and Suitability. Int J Hydrogen Energy 2014;39:20434–9. https://doi.org/10.1016/j.ijhydene.2014.03.234

[18] San Marchi C, Yamabe J, Schwarz M, Matsunaga H, Zickler S, Matsuoka S, Kobayashi H. Global Harmonization of Fatigue Life Testing in Gaseous Hydrogen. ASME PVP2018-84898; 2018. https://doi.org/10.1115/PVP2018-84898

[19] Yamabe J, Matsunaga H, Furuya Y, Hamada S, Itoga H, Yoshikawa M, Takeuchi E, Matsuoka S. Qualification of chromium–molybdenum steel based on the safety factor multiplier method in CHMC1-2014. Int J Hydrogen Energy 2015;40:719–28. https://doi.org/10.1016/j.ijhydene.2014.10.114

[20] Matsuoka S, Yamabe J, Matsunaga H. Criteria for determining hydrogen compatibility and the mechanisms for hydrogen-assisted surface crack growth in austenitic stainless steels. Eng Fract Mech 2016;153:103–27. https://doi.org/10.1016/j.engfracmech.2015.12.023

[21] Yamabe J, Itoga H, Awane T, Matsuo T, Matsunaga H, Matsuoka S. Pressure cycle testing of Cr-Mo steel pressure vessels subjected to gaseous hydrogen. J Pres Ves Technol 2016;138-011401:1–13. https://doi.org/10.1115/1.4030086

[22] Nakamura J, Omura T, Tomio Y, Hirata H, Terunuma M, Dan E, Osuki T. Mechanical properties of high nitrogen – high strength stainless steels in high pressure gaseous hydrogen environment. ASME PVP2013-97365; 2013. https://doi.org/10.1115/PVP2013-97365

[23] Kubota J, Watanabe Y. Mechanical properties and room-temperature creep deformation of hydrogen-charged low-Mo austenitic stainless steels for high-pressure hydrogen use. J Japan Inst Met Mater 2015;79:100–6 (in Japanese). https://doi.org/10.2320/jinstmet.JC201403

[24] Yamabe J, Takagoshi D, Matsunaga H, Matsuoka S, Ishikawa T, Ichigi T. High-strength copper-based alloy with excellent resistance to hydrogen embrittlement. Int J Hydrogen Energy 2016;41:15089–94. https://doi.org/10.1016/j.ijhydene.2016.05.156

[25] Ogawa Y, Yamabe J, Matsunaga H, Matsuoka S. Material performance of age-hardened beryllium-copper alloy, CDA-C17200, in a high-pressure, gaseous hydrogen environment. Int J Hydrogen Energy 2017;42:16887–900. https://doi.org/10.1016/j.ijhydene.2017.04.270

[26] Wada K, Yamabe J, Takakuwa O, Iijima T, Matsunaga H. Comparative study of hydrogen-induced intergranular fracture behavior in Ni and Cu–Ni alloy at ambient and cryogenic temperatures. Mater Sci Eng A 2019;766:138349. https://doi.org/10.1016/j.msea.2019.138349

[27] Wada K, Yamabe J. The effect of the Ni/Cu ratio on H-induced ductility loss and its mechanism in Cu–Ni binary alloy system. Int J Hydrogen Energy 2021;46:39577–89. https://doi.org/10.1016/j.ijhydene.2021.09.140

[28] Michler T, Naumann J. Influence of high pressure hydrogen on the tensile and fatigue properties of a high strength Cu-Al-Ni-Fe alloy. Int J Hydrogen Energy 35;2010:11373-7. https://doi.org/10.1016/j.ijhydene.2010.07.093

[29] Culpan EA, Rose G. Microstructural characterization of cast nickel aluminium bronze. J Mater Sci 1978;13:1647–57. https://doi.org/10.1007/BF00548728

[30] Brezina P. Heat treatment of complex aluminium bronzes. Int Met Rev 1982;27:77–120. https://doi.org/10.1179/imr.1982.27.1.77

[31] Al-Hashem A, Riad W. The role of microstructure of nickel-aluminium-bronze alloy on its cavitation corrosion behavior in natural seawater. Mater Charat 2002;48:37–41. https://doi.org/10.1016/S1044-5803(02)00196-1

[32] Demarez A, Hock AG, Meunier FA. Diffusion of hydrogen in mild steel. Acta Metall 1954;2:214–23. https://doi.org/10.1016/0001-6160(54)90162-5

[33] Matsuo T, Yamabe J, Furukawa H, Seki K, Shimizu K, Watanabe S, Matsuoka S. Development of New Strain Gage for High-Pressure Hydrogen Gas Use. Exp Mech 2014;54:431–42. https://doi.org/10.1007/s11340-013-9816-4

[34] Yamabe J, Awane T, Matsuoka S. Investigation of hydrogen transport behavior of various low-alloy steels with high-pressure hydrogen gas. Int J Hydrogen Energy 2015;40:11075–86. https://doi.org/10.1016/j.ijhydene.2015.07.006

[35] Wada K, Yamabe J, Matsunaga H. Mechanism of hydrogen-induced hardening in pure nickel and in a copper-nickel alloy analyzed by micro Vickers hardness testing. Mater Sci Eng A 2021;805:140580. https://doi.org/10.1016/j.msea.2020.140580

[36] Cook M, Fentiman WP, Davis E. Observations on the Structure and Properties of Wrought Copper-Aluminum-Nickel-Iron Alloys. J Inst Met 1951–2;80:419–29.

[37] Japan Society for the Promotion of Science. Aluminum Bronze (1967) THE NIKKAN KOGYO SHIMBUN, LTD (in Japanese).

[38] Kanamori M, Ueda S, Matsuo S. On the Structures of Cu-A1-Ni-Fe cast alloys. J Japan Inst Met Mater 1962;24:201-5 (in Japanese). https://doi.org/10.2320/jinstmet1952.24.4_201

[39] Hagi H. Diffusion Coefficients of Hydrogen in Ni–Cu and Ni–Co Alloys. Trans Jpn Inst Met 1986;27:233-40. https://doi.org/10.2320/matertrans1960.27.233